ELSEVIER

Materials Science and Engineering A 390 (2005) 188–201

MATERIALS SCIENCE & ENGINEERING A

www.elsevier.com/locate/msea

Mathematical modeling of residual stress formation in electron beam remelting and refining of scrap silicon for the production of solar-grade silicon

D.M. Maijer[a,*], T. Ikeda[b], S.L. Cockcroft[a], M. Maeda[b], R.B. Rogge[c]

[a] *Department of Metals and Materials Engineering, The University of British Columbia, 309-6350 Stores Road, Vancouver, BC, Canada*
[b] *Institute of Industrial Science, The University of Tokyo, 7-22-1 Roppongi, Minato, Tokyo, Japan*
[c] *Neutron Program for Materials Research, National Research Council, Canada, Chalk River Laboratories, Chalk River, Ont., Canada*

Received 7 June 2004; accepted 14 August 2004

Abstract

A technique based on electron beam melting and refining has been used to refine N-type scrap silicon for the purpose of producing material suitable for photovoltaic applications. In this paper, the experimental setup and methodology are described and are presented together with the experimental results for three experiments. Temperature data obtained from embedded thermocouples for one of the experiments is presented. Neutron diffraction analysis was employed to measure the residual strain in the three castings. Finite element thermal and stress mathematical models are employed to predict the residual stress distribution.

Keywords: Electron beam melting and refining; Silicon; Mathematical modeling; Solidification; Heat transfer; Residual stress; Neutron diffraction

1. Introduction and background

The wide spread use of solar-cells for power generation remains impractical for a number of reasons, including their low energy conversion efficiencies and their high cost relative to conventional fossil fuels. While work is ongoing to improve their efficiency, effort must also be applied to reduce fabrication costs, which in turn, will depend to a large extent on a low-cost source of solar-grade silicon. Presently, the purity required for solar-grade silicon is around seven nines and the main source is expensive semiconductor-grade silicon [1].

The total production of solar-cells in Japan, as indicated by generating capacity, increased from 20 MW in 1996 to 80 MW in 1999. In 1999, the production of solar-cells from crystalline silicon was approximately 69 MW, comprising 85% of total production, with the balance being produced from cells based on multi-crystalline silicon [2]. However, during the period 1996 to 1999 there was proportionally a larger increase in the multi-crystalline silicon type cell.

P- and N-type silicon are produced for semi-conductor device manufacturing. Most of this material is produced in single crystal form using either the floating zone (FZ) method or the Czochralski (CZ) method. According to the statistics, the amount of scrap silicon produced from the CZ process is sufficient to supply the solar-cell market if a suitable cost-effective processing route can be found to remove the dopant.

Previous experimental investigations have been conducted on a number of different purification methods for metallurgical grade silicon including: vacuum distillation for removal of phosphorous and plasma treatment to remove boron by Suzuki et al. [3]; filtration and oxidation of carbon by Sakaguchi and Maeda [4]; filtration of carbon by Suhara et al. [5]; blowing by argon to remove carbon by Yuge [6]; and, electron beam (EB) button distillation of carbon, phosphorous, calcium and aluminum by Ikeda and Maeda [7]. The work of Ikeda and Maeda [7], has clearly demonstrated the

* Corresponding author. Tel.: +1 604 822 6013; fax: +1 604 822 3619.
E-mail address: daan@cmpe.ubc.ca (D.M. Maijer).

0921-5093/$ – see front matter © 2004 Elsevier B.V. All rights reserved.
doi:10.1016/j.msea.2004.08.036

Nomenclature

C	pre-exponential EB gun heat flux constant ($W m^{-2}$)
C_{melt}	pre-exponential heating and melting heat flux constant ($W m^{-2}$)
C_p	specific heat ($J kg^{-1} K^{-1}$)
d	lattice spacing (Å)
h_{copper}	copper to cooling water heat transfer coefficient ($W m^{-2} K^{-1}$)
$h_{graphite/copper}$	interfacial heat coefficient for the graphite/copper interface ($W m^{-2} K^{-1}$)
$h_{ingot/graphite}$	interfacial heat coefficient for the ingot/graphite interface ($W m^{-2} K^{-1}$)
h_{side}	ingot side heat transfer coefficient ($W m^{-2} K^{-1}$)
$\Delta H_{melting}$	heat of melting of silicon ($J kg^{-1}$)
k	thermal conductivity ($W m^{-1} K^{-1}$)
$\dot{m}_{Si}$	melt rate of the silicon ($kg s^{-1}$)
P_{EB}	total EB gun power (W)
P_{melt}	power to heat and melt silicon (W)
q_{EB}	EB gun heat flux ($W m^{-2}$)
q_{melt}	heat flux correction for heating and melting silicon ($W m^{-2}$)
q_{rad}	radiative heat flux ($W m^{-2}$)
q_s	effective surface heat flux ($W m^{-2}$)
$\dot{Q}$	volumetric latent heat ($W m^{-3}$)
r	radius (m)
R_0	outer radius of ingot (m)
s	Stephan–Boltzman constant 5.6695×10^{-8} ($W m^{-2} K^{-2}$)
t	time (s)
T	temperature (K)
T_s	surface temperature of ingot (K)
T_∞	far-field radiation or surrounding environment temperature (K)
z	axial height (m)

Greek letters

α	coefficient of linear expansion (K^{-1})
ε	emissivity of silicon
ε_{th}	thermal strain
η_{power}	normalized EB power
θ	Bragg angle (°)
λ	incident beam wavelength (Å)
μ_{EB}	EB power transfer efficiency
ρ	density ($kg m^{-3}$)
σ	standard deviation of the EB gun heat flux distribution (m^2)

efficacy of the EB cold hearth re-melting process to reduce the volatile species, apart from boron, to acceptable levels (it would appear at the present time, that an initial plasma treatment to remove boron is needed prior to electron beam processing).

Independent of the refining methodology used, it is clear that the development of dislocations and micro cracks during consolidation has a negative impact on solar-cell efficiency [8], hence, it is critical that the solidification processing step minimize their occurrence.

This paper presents the development and validation of a finite element (FE) based mathematical model to predict the evolution of the temperature and stress during electron beam melting and refining (EBMR) of solar-grade silicon ingots. In this study, three small ingots were produced under different conditions in a laboratory scale EB furnace. The thermal component of the model has been validated against thermocouple measurements and the calculated strains have been compared to residual strain measurements obtained from neutron diffraction data.

2. Experimental

2.1. Feed material characterization

As previous work [7] has established that the EB process cannot be used to remove boron, N-type scrap was chosen. (P-type silicon uses mainly boron and N-type silicon uses phosphorus, arsenic or antimony for doping.) The choice to use antimony-doped scrap was made owing to its availability. The feed material used in the experiments was crushed (fractured) using a quench based process to produce a granular feedstock with average size of the order of 5–10 mm. The raw material prior to fracturing was taken from a combination of top and tail scrap from a single crystal boule. Fig. 1 illustrates schematically the sources of scrap arising from the

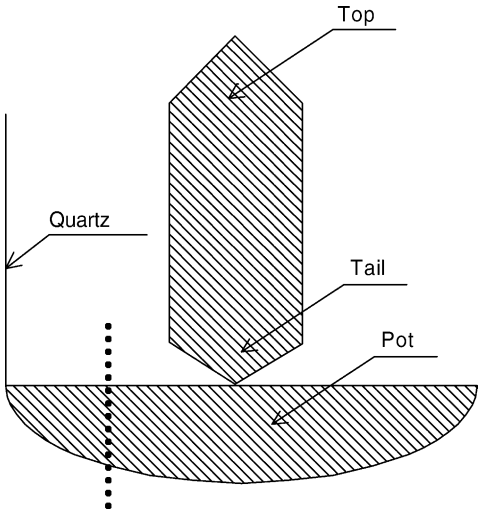

Fig. 1. Schematic of scrap sections arising from the CZ process.

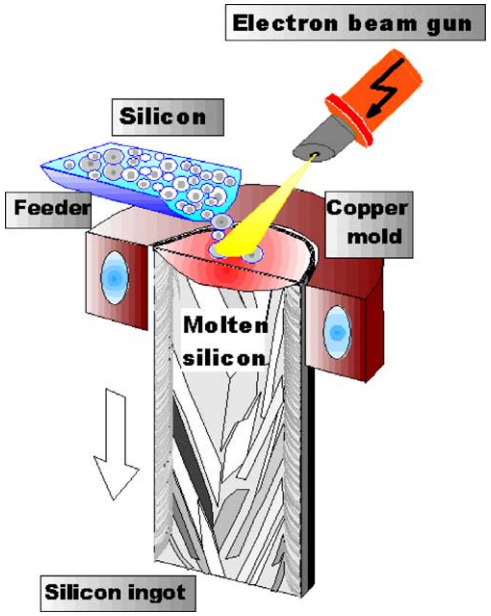

Fig. 2. Schematic illustration of electron beam casting process.

CZ process. The induction coupled plasma technique (Seiko Instrument Inc. SPS 4000) was used to characterize the feedstock which was found to typically contain about 10000 ppm antimony. The resistivity of this material, measured using the four-point probe method (NAPSON Corp. RT-7 tester and RG-5 stage), was found to be generally less than about 10 mΩ cm. A typical target value for a solar-cell application is greater than 10 Ω cm, or about three orders of magnitude greater than the top and tail material. Hence the need for EBMR of CZ scrap.

2.2. Experimental equipment

Fig. 2 schematically illustrates the basic layout of the experimental equipment including the EB gun, vibratory feeder and water-cooled copper mould. Fig. 3 shows in more detail

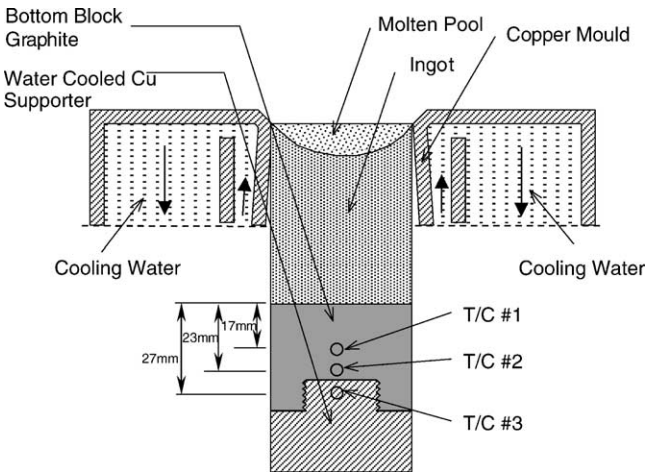

Fig. 3. Schematic cross sectional view of mould and ingot assembly.

the mould assembly, the bottom block and supporter. The water-cooled copper mould was 40 mm in diameter at the top and was tapered outward toward the bottom to accommodate the expansion of silicon that occurs during solidification (approximately 9.5%) [9].

Typically in solidification processes of this type, the bottom, or starter, block is made of the same material being cast to avoid issues associated with differential thermal contraction. However, silicon cannot be readily manufactured into the starter block shape because of its brittleness. Graphite was selected as an alternative material for the starter block owing to its high melting point and low reactivity with molten silicon. The supporter was made from copper and was water-cooled. The graphite bottom block was screwed to the copper support to facilitate mechanical contact, to allow withdrawal of the ingot from the mould, and good thermal contact, promoting directional solidification.

Three Type-K thermocouples, 0.2 mm in diameter, were embedded into the graphite starting block and copper support structure along the centerline, as shown in Fig. 3. Thermocouples placed in the graphite were located 17 and 23 mm from the silicon/graphite interface. The third thermocouple was located 5 mm from the graphite/copper interface. A two-color optical pyrometer was used to measure the pool surface temperature. The pyrometer was initially calibrated using the freezing point of pure silicon (1412 °C) and was found to agree well. However, problems persisted with its use during the actual casting process likely owing to the fact that the cold material charged to the melt was intermittently in the field of view making acquisition of a representative melt surface temperature difficult.

The entire assembly was placed in a vacuum chamber to facilitate operation of the EB gun. The furnace chamber has a volume of 0.06 m^3 and is equipped with a single EB gun with a maximum power of 8 kW. The chamber is evacuated with a combination of a rotary pump, of capacity 1.08 m^3/s and a turbo molecular pump, of capacity 1 m^3/s. The gun is separated from the melting chamber by an orifice and evacuated with a small turbo molecular pump, of capacity 0.05 m^3/s, in order to maintain the gun atmosphere under 10^{-2} Pa. The furnace chamber is water-cooled and has two large view ports positioned to permit the observation of melting and feeding both visually and/or with a pyrometer. The view ports are equipped with glass disk vapor shields that can be rotated when excessively coated with deposited vapor. In addition, the furnace is also equipped with a feeder (for the addition of particulate or consolidated feedstock), a water-cooled copper mold and a screw auger located below the mold (to permit an ingot to be withdrawn).

2.3. Experimental procedure

The experimental procedure involved the following steps:

1. The chamber was pumped down to a pressure of 10^{-2} Pa.

Table 1
Summary of casting conditions

Casting number	Power input (kW)	Ingot withdrawal rate (mm/min)
1	3.8	2
2	3.8	1
3	5.0	2

2. The beam power was then switched on and the top surface of the graphite starting block was preheated until the desired temperature was reached (as estimated from the thermocouples embedded in the graphite).
3. A small amount of silicon feed was then introduced into the mold and simultaneously the power was increased to the desired level, until a stable molten pool was achieved.
4. The starting block was then lowered at the desired rate while adding particulate silicon at a rate sufficient to maintain the desired molten pool level in the mould. This process was continued until the desired ingot length was reached, typically between 40 and 60 mm.

During each experiment, data from the three thermocouples was logged together with the beam power and the output from the pyrometer. The ingot withdrawal rate was also recorded.

To examine the effect of beam power and withdrawal rate on residual stress development, three ingots were produced using different casting conditions as summarized in Table 1. Fig. 4 shows the typical solidified microstructure in an ingot following sectioning and etching. The grain size ranges from the order of 0.1 mm at the surface to the order of 10 mm in the interior. The morphology is columnar throughout, with the orientation radial on the vertical sides of the ingot and axial along the bottom and up the center.

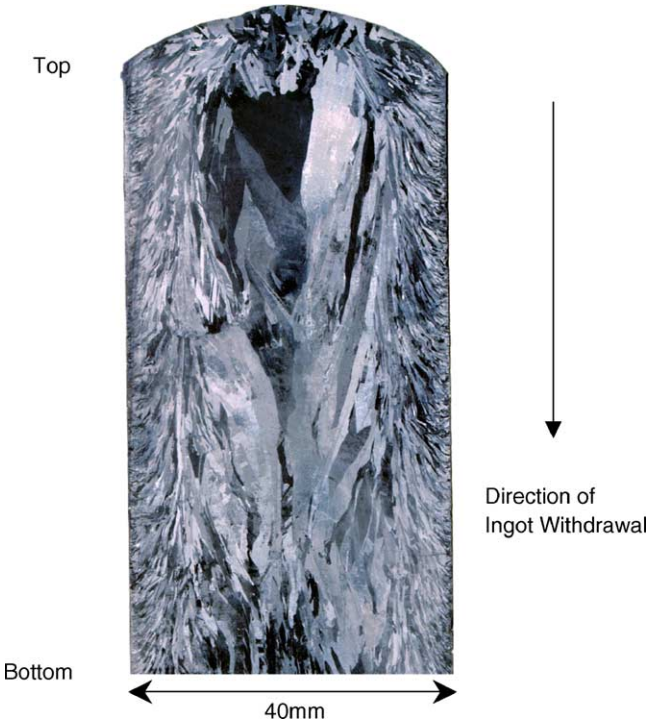

Fig. 4. Etched cross section of silicon ingot.

2.4. Residual stress measurement

The residual stress in the three ingots produced in this study was measured via the neutron diffraction technique at the National Research Council's (NRC) Neutron Program for Materials Research (NPMR) laboratory in Chalk River, Ontario, Canada. The ingots included the graphite starter block which was stuck to the base of the ingot following completion of the casting process (*Note*: The graphite starter block was not removed as it would have altered the distribution of residual stresses arising from the casting process). A full discussion of the details of this technique is beyond the scope of this paper, but may be found in [10]. The technique of measuring residual stresses via neutron diffraction centres on measuring the angle of diffraction of an incident neutron beam striking a sample, which is normally held stationary. It can be seen from Bragg's Law, Eq. (1), that it is possible to determine the average lattice spacing for the material within the intersection volume of the incident and diffracted beams:

$$\lambda = 2d \sin\theta \quad (1)$$

where λ is the incident beam wavelength in (0.1544 nm for these experiments), d the lattice spacing, and θ the Bragg angle. Due to the penetration of neutrons, it is possible to position this sampling volume at locations of interest within the material. The lattice strain is defined as the change in lattice spacing relative to the lattice spacing of unstressed material. The component of strain determined by diffraction corresponds to the sample direction parallel to the bisector of the incident and diffracted beams. After determining the strain in at least three mutually orthogonal directions, it is possible to calculate the stress for the material in those same directions at a particular location within the sample.

The conventional neutron diffraction technique is best suited to materials with fine homogeneous grain sizes (typically less than 80 μm). In these materials, the incident beam strikes a multitude of grains ensuring a good statistical sampling of the macroscopic residual strain at each location. Conversely, when large grains are present in a sample, the measurement no longer provides a suitable statistical sampling, increasing the uncertainty of the measurement. In the extreme case where only one grain is being sampled, the grain must be correctly oriented to obtain an accurate measurement of the lattice spacing. Unfortunately in the present investigation, some of the grains in the centre of the ingot are large and all show a preferred orientation along the direction of heat flow—refer to Fig. 4. However, at a given axial position, the grain size and orientation distributions are circularly symmetric. As well, it is anticipated that the EB solidification process will lead to stress distributions sharing this symmetry. Thus it was possible to average over many grains by

Table 2
Estimated strain measurement uncertainty range (in microstrain)

Casting number	Stain measurement uncertainty range ($\mu\varepsilon$)		
	Radial	Hoop	Axial
1	±128–424	±48–139	±88–341
2	±50–96	±47–109	±52–95
3	±41–100	±64–123	±52–200

continuously spinning the sample about its axis while obtaining the diffraction peak at each radial and axial position. Nevertheless, it is acknowledged that as the grain size increases (say to ∼300 μm) this averaging will again fail to provide good statistical quality data. Measurements of the residual strain in the radial, axial and hoop orientations were performed at a number of different radial and axial locations.

The uncertainty of the individual measurements can be traced back to the quality of fit of the diffraction data. The uncertainties for most measurements fall within the typical range of 50–150 $\mu\varepsilon$ for diffraction measurements. For some measurements however, the uncertainty is considerably greater due to the large grain effects, inhomogeneous nature of the grain structure in the casting, and the presence of voids. Table 2 summarizes the estimated strain measurement uncertainty. The measured strain data will be presented along with the results of the model predictions following a description of the mathematical model formulation.

3. Mathematical model development

The development of the overall thermal-stress mathematical model is presented in two sections—(1) the thermal model and (2) the mechanical or stress model. The models are sequentially coupled, with the thermal field being calculated first to provide input to the stress analysis.

3.1. 2D axisymmetric finite element heat transfer model

A finite element (FE) based heat transfer model was developed to describe the heat transfer occurring in the ingot, bottom block and copper support. The model was intended to serve two purposes: (1) to predict the depth of the liquid pool and (2) to predict the evolution in the thermal field within the ingot and bottom block which is needed for input to the thermal-stress model.

The commercial finite element package ABAQUS™[1] was used as a platform for development and solution of the problem. It has been assumed that the heat flow in the process is symmetric in the circumferential direction. The 2D axisymmetric mesh used in the analysis, shown in Fig. 5, contains 2393 nodes and 2210 linear temperature elements. As the casting process involves the continuous withdrawal and formation of the ingot, this is modeled by incrementally adding the layers of the elements within the ingot in a manner consistent with the process—i.e. all of the ingot element layers are initially removed from the model to allow preheating of the starter block and the layers are then added back to the analysis at a rate consistent with the withdrawal rate of the ingot.

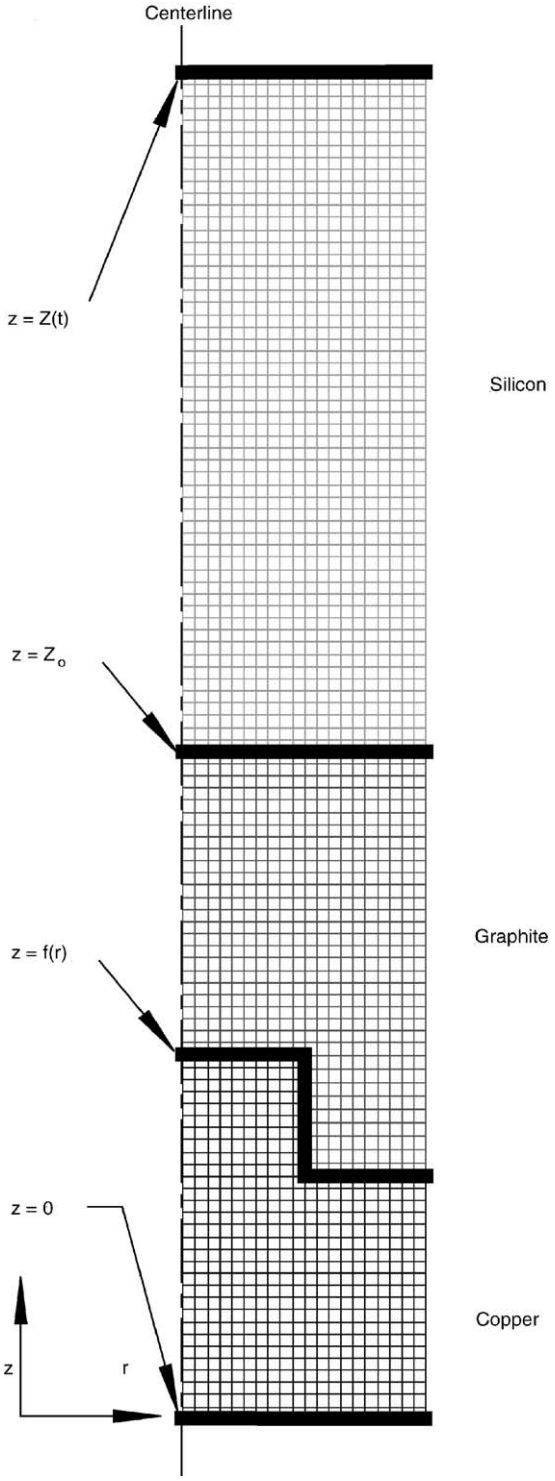

Fig. 5. Finite element mesh of the silicon, graphite starter block and copper support.

[1] ABAQUS is a trademark of Abaqus Inc.

In view of the above assumptions, the flow of heat in the ingot, starter block and copper support in the radial direction, r, and in the axial direction, z, can be described as follows:

$$\frac{1}{r}\frac{\partial}{\partial r}\left(kr\frac{\partial T}{\partial r}\right)+\frac{\partial}{\partial z}\left(k\frac{\partial T}{\partial z}\right)+\dot{Q}=\rho C_{\mathrm{p}}\frac{\partial T}{\partial t} \quad (2)$$

where T (K) the temperature, r (m) the radius, z (m) axial height, k (W/m K) the thermal conductivity, ρ (kg/m^3) the density, C_{p} (J/kg K) the specific heat, and $\dot{Q}$ (W/m^3) the volumetric latent heat associated with the solidification phase transformation (this term is set to zero in the starter block and in the copper support).

The top surface of the mesh is subject to irradiation by the electron beam, which is treated as a spatially and temporally dependent surface heat flux:

$$-k\left.\frac{\partial T}{\partial z}\right|_{z=Z(t)}=q_{\mathrm{s}},\quad \text{for } t>0 \text{ and } z=z(t) \quad (3)$$

where q_{s} (W/m^2 K) is the effective surface heat flux. The intensity of q_{s} is a function of the EB power applied, the radiative losses, and a correction term for the heat required to raise the temperature of the silicon to the initial condition temperature of 1412 °C. The input heat flux from the EB gun, q_{EB} (W/m^2) has been described using a Gauss function, Eq. (4):

$$q_{\mathrm{EB}}=\mu_{\mathrm{EB}}\,\eta_{\mathrm{power}}C\mathrm{e}^{[-r^2/2\sigma^2]} \quad (4)$$

where μ_{EB} is the EB power transfer efficiency, η_{power} the normalized EB power, C (W/m^2) a pre-exponential constant, r (m) the radius, and σ (m) the standard deviation of the distribution. The total beam power is obtained by integrating Eq. (4) across the ingot surface radially from 0 to R_0 and circumferentially from 0 to 2π with μ_{EB} and η_{power} set to 1. Integration of Eq. (4) yields the total gun power, P_{EB} (W), shown in Eq. (5).

$$P_{\mathrm{EB}}=2\pi C\sigma(1-\mathrm{e}^{-R_0^2/2\sigma^2}) \quad (5)$$

Using Eq. (5), the constant C is chosen to ensure the correct total beam power for a given value of σ. For example, when σ is 0.00005 and the input power P = 1000 W, C is 3,242,487 W/m^2. The EB power factor η_{power}, normalized to 1000 W, is input to the model in tabulated form and is obtained from the data acquired during each casting. For example, η_{power} is 3 for an EB power setting of 3 kW.

The input power from the EB gun applied to the top surface during casting is reduced by an amount equal to the power required to heat and melt the silicon at a rate consistent with the casting speed as follows:

$$P_{\mathrm{melt}}=\dot{m}_{\mathrm{Si}}\left[\int_{298}^{1685}C_{\mathrm{p}}\,\mathrm{d}T+\Delta H_{\mathrm{melting}}\right] \quad (6)$$

where $\dot{m}_{\mathrm{Si}}$ (kg/s) is the melt rate of the silicon and $\Delta H_{\mathrm{melting}}$ (J/kg) is the heat of melting. Rather than applying a uniform heat flux correction across the top surface of the silicon which results in negative heat flux values at outer regions of the ingot, a heat flux correction, q_{melt} (W/m^2), based on the Gaussian EB heat flux equation (refer to Eq. (4)) has been applied as follows:

$$q_{\mathrm{melt}}=C_{\mathrm{melt}}\mathrm{e}^{[-r^2/2\sigma^2]} \quad (7)$$

C_{melt} (W/m^2) is chosen to ensure the correct total beam power for a given value of σ and $\dot{m}_{\mathrm{Si}}$. For example, when σ is 0.00005 and $\dot{m}_{\mathrm{Si}}$ is 0.1×10^{-3} kg/s (withdrawal rate of 1 mm/s), C_{melt} is 509,070 W/m^2.

The radiative losses of the top surface of the silicon, q_{rad} (W/m^2), are described with a far-field radiation equation of the form:

$$q_{\mathrm{rad}}=\varepsilon\sigma(T^4-T_\infty^4) \quad (8)$$

where ε is the emissivity of the silicon surface, σ (5.6695×10^{-8} W/m^2 K^4) is the Stephan–Boltzman constant, and T_∞ (K) is the far-field temperature. Overall, the heat flux, q_{s}, applied to the top surface of the silicon is the sum of the three terms, $q_{\mathrm{EB}}+q_{\mathrm{melt}}+q_{\mathrm{rad}}$.

The outer radius of the ingot, $z\geq Z_0$, $r=R_0$, is subject to various rates of heat transfer depending on whether the region of interest is within the meniscus region of the mould or is in the gap region located below [11–13]. This boundary condition has the general form:

$$-k\left.\frac{\partial T}{\partial r}\right|_{r=R_0}=h_{\mathrm{side}}(T_{\mathrm{s}}-T_\infty),\quad \text{for } t>0 \text{ and } r=R_0 \quad (9)$$

where h_{side} (W/m^2 K) is the ingot side heat transfer coefficient, T_{s} the surface temperature of the ingot, and T_∞ is the temperature of the surrounding environment. These various regimes of heat transfer that Eq. (9) represents are calculated by specifying a heat transfer coefficient which is a function of temperature using an approach similar to others appearing in the literature [11–13]. Table 3 summarizes the heat transfer coefficients and their regions of application along the ingot side. The magnitude of h_{max} is similar to that adopted by Ritchie et al. [13]. Fine tuning of h_{max} and its variation with temperature for this application was achieved through a process of trial and error fitting of the model to the measured thermocouple data.

For positions below the ingot, $z<Z_0$, $r=R_0$, representing the side of the graphite starter block, Eq. (9) was also applied however, the h_{cond} term appearing in Table 3 was set to zero as only radiation heat transport is assumed to occur.

Interfacial heat transfer boundary conditions of the Cauchy type are applied along the interface between the ingot and the graphite starter block and along the interface between the graphite starter block and the copper support block as follows:

$$-k\left.\frac{\partial T}{\partial z}\right|_{z=Z_0}=h_{\mathrm{ingot/graphite}}(T_{\mathrm{ingot}}-T_{\mathrm{graphite}}),\quad \text{for } t>0 \text{ and } z=Z_0 \quad (10)$$

Table 3
Summary of boundary conditions applied in thermal model

Boundary conditions	
Heat loss from: the side of the ingot ($z > Z_0$), and the graphite and copper ($z < Z_0$)	$h_{side} = h_{cond} + h_{rad}, \quad T_\infty = 8^\circ$ C $h_{cond} = \begin{cases} \begin{cases} h_{max} & \text{if } T_s > 1400\,^\circ\text{C} \\ h_{max} f_{cond} & \text{if } 1300\,^\circ\text{C} \le T_s \le 1400\,^\circ\text{C} \\ 0 & \text{if } t < 1300\,^\circ\text{C} \end{cases} & \text{if } z > Z_0 \\ 0 & \text{if } z < Z_0 \end{cases}$ $f_{cond} = \frac{T_s - 1300\,^\circ\text{C}}{1400\,^\circ\text{C} - 1300\,^\circ\text{C}}, \quad h_{max} = 2500\,\text{W/m}^2\,\text{K}$ $h_{rad} = \sigma\varepsilon(T_s^4 - T_\infty^4)$ $\varepsilon_{ingot} = 0.5$, $\varepsilon_{graphite} = \varepsilon_{copper} = 0.85$
Heat transfer between the bottom surface of the ingot/the top surface of the graphite starter block	$h_{ingot/graphite} = \begin{cases} (h_{mid} - h_{min}) f_{mid/min} + h_{min}, & \text{if } t < 700\,\text{s} \\ (h_{max} - h_{mid}) f_{max/mid} + h_{mid}, & \text{if } 700\,\text{s} \le t < 720\,\text{s} \\ h_{max} & \text{if } t > 720\,\text{s} \end{cases}$ $f_{mid/min} = \frac{t}{700}, \quad \text{if } t < 700\,\text{s}$ $f_{min/mid} = \frac{t - 700\,\text{s}}{720\,\text{s} - 700\,\text{s}}, \quad \text{if } 700\,\text{s} \le t < 720\,\text{s}$ $h_{min} = 200\,\text{W/m}^2\,\text{K}$, $h_{mid} = 1500\,\text{W/m}^2\,\text{K}$, $h_{max} = 4000\,\text{W/m}^2\,\text{K}$
Heat transfer between the bottom surface of the graphite starter block/top surface of the copper	$h_{graphite/copper} = 500\,\text{W/m}^2\,\text{K}$
Heat loss from the bottom of the copper	$h_{copper} = 4000\,\text{W/m}^2\,\text{K}, \quad T_\infty = 8\,^\circ$C

$$-k\left.\frac{\partial T}{\partial z}\right|_{z=f(r)} = h_{graphite/copper}(T_{graphite} - T_{copper}),$$
$$\text{for } t > 0 \text{ and } z = f(r) \tag{11}$$

where $h_{ingot/graphite}$ and $h_{graphite/copper}$ (W/m^2 K) are the interfacial heat transfer coefficients for the ingot/graphite and graphite/copper interfaces, respectively. The values of these interfacial heat transfer coefficients are summarized in Table 3.

Initially, it was assumed that the interfacial heat transfer coefficient between the ingot and graphite surfaces was constant. However, it was apparent, based on a comparison between the model predictions and the measured temperature, that heat transfer across this interface started low, increased and then decreased with time. This behavior may be rationalized as follows: initially the heat transfer is low because the granular feedstock has a relatively low contact area with the graphite. Once it melts this contact area increases resulting in increased heat transfer. As the cast length increases and the base of the ingot cools a gap forms due to thermal contraction of the silicon resulting in a decreased in the heat transfer across the interface. Consequently, the interfacial heat transfer coefficient along this interface was defined as a function of time to mimic the poor initial heat transport. The values of $h_{ingot/graphite}$ shown in Table 3 and their variation with time were defined by fitting to the measured temperature in the graphite and copper.

The Cauchy type boundary condition applied along the base of the copper support to simulate heat transfer to the cooling water is given in Eq. (12).

$$-k\left.\frac{\partial T}{\partial z}\right|_{z=0} = h_{copper}(T_s - T_\infty), \quad \text{for } t > 0 \text{ and } z = 0 \tag{12}$$

where h_{copper} (W/m^2/K) is the heat transfer coefficient between the copper and cooling water, and T_∞ (K) is the cooling water temperature. The copper to water heat transfer coefficient and the water temperature are summarized in Table 3.

For the ingot, the initial temperature of the layers of elements added to the model is set equal to the melting point of silicon, 1412 °C. The initial temperatures of the graphite starter block and copper support block are set equal to 25 °C.

The baseline material properties input to the model are presented in Table 4. These data are input to ABAQUS in a tabulated form and linear interpolation is used for evaluation at temperatures that lie between the discrete points. Silicon, of the composition present in this study, has essentially a unique melting/solidification temperature, 1412 °C. To ease convergence and reduce execution time the latent heat of solidification, 1,803,778 J/kg [14], is released linearly with temperature over a solidification temperature range from 1400 to 1412 °C.

3.2. 2D axisymmetric finite element thermal-stress model

The evolution of stresses in the ingot has been determined using a thermal-stress model also developed in ABAQUS. The stress model solves the differential equations of equilibrium based on a force balance on an elemental volume and the compatibility conditions based on the displacement field and its relationship to strain in the body. The FEM equations can be developed through the minimization of virtual work within an element [15]. The temperature predictions obtained from the thermal model serve as 'thermal loads' input to the stress model in place of mechanical loads normally appearing in a structural analysis. In addition, since the 'thermal loads' dominate the mechanical response of the ingot the influence of gravity on the stress distribution has been neglected.

Table 4
Thermo-physical properties of silicon, graphite, and copper [14,16,17]

Material	ρ (kg/m^3)	Temperature (°C)	C_p (J/kg K)	Temperature (°C)	k (W/m K)
Silicon	2330	27	713	27.0	148.0
		127	785	77.0	119.0
		227	832	127.0	98.9
		327	849	227.0	76.2
		527	883	327.0	61.9
		727	916	527.0	42.2
		927	950	727.0	31.2
		1127	983	927.0	25.7
		1327	1017	1127	23.5
		1412	1031	1327	22.1
				1412	22.1
				1450	100.0
Graphite	1690	17	838	27	129
		129	1048	77	124
		207	1257	127	118
		304	1383	227	106
		449	1508	327	95
		521	1592	427	85
		631	1676	527	77
		720	1718	627	70
		829	1760	727	64
		1652	1760	927	55
				1127	49
				1327	45
				1527	42
				1727	40
				1927	38
				2127	36
Copper	8960		398		393

The model uses an elastic-perfectly plastic formulation and is based on the assumption that the in-elastic behaviour of silicon, particularly at elevated temperatures, can be adequately described by Von Mises metal plasticity in which the flow stress is temperature dependent. The graphite block has been included in the analysis because the ingot is typically bonded to it at the end of the casting process. The copper support block does not influence the stress in the ingot and accordingly, has been ignored.

The solution of the thermal-stress problem requires quantification of a variety of mechanical properties over the temperature range experienced in the casting process, including the elastic modulus, Poisson's ratio, stress-strain response and thermal dilatational behavior. The elastic modulus and Poisson's ratio data required for the stress analysis, for both graphite and silicon, appear in Table 5. The variation in flow stress with temperature for the silicon has been plotted in Fig. 6 over a range of temperatures. As can be seen, the mechanical behaviour of silicon exhibits strong temperature dependence at elevated temperature. The in-elastic response of the material is assumed to be symmetric in compression and in tension, consistent with Von Mises metal plasticity. The data is input to ABAQUS in a tabulated form and linear interpolation is used for evaluation at temperatures that lie between the discrete points.

As previously discussed, interaction with the surrounding mold materials apart from the graphite starting block has been neglected. The symmetry boundary used in the stress model follows directly from the assumption of axial symmetry in the heat transfer model. Therefore, displacement in the direction normal to the vertical centerline of the casting has been assumed to be zero as the thermally induced loads normal to the symmetry boundary would be equal and opposite.

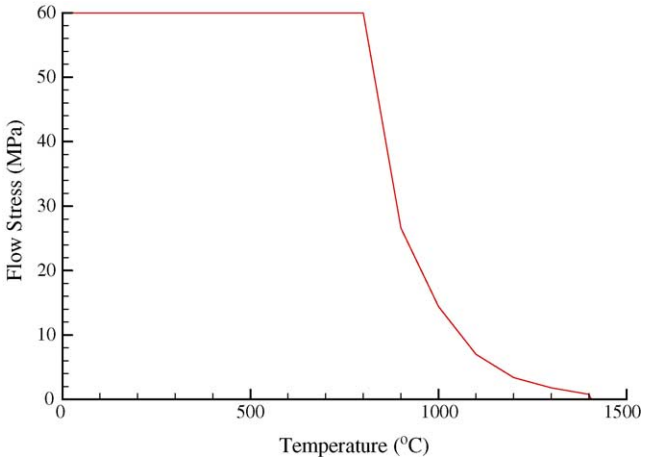

Fig. 6. Flow stress vs. temperature for a strain rate of $1.2 \times 10^{-4}\,s^{-1}$ [19].

Table 5
Mechanical properties of poly-crystalline silicon and graphite [14,18]

Material	ν	Temperature (°C)	E (MPa)
Silicon	0.22	25	16.57
		125	16.42
		225	16.28
		325	16.14
		425	16.00
		525	15.86
		625	15.72
		725	15.58
		825	15.45
		925	15.31
		1025	15.18
		1125	15.05
		1225	14.91
		1325	14.78
		1400	1.0×10^{-4}
		1406	1.0×10^{-5}
		1412	1.0×10^{-6}
Graphite	0.3	21	2.66×10^{4}
		260	2.79×10^{4}
		538	2.93×10^{4}
		816	3.09×10^{4}
		1093	3.24×10^{4}
		1371	3.52×10^{4}
		1649	3.81×10^{4}
		1927	1.34×10^{4}
		2204	1.21×10^{4}
		2482	1.00×10^{4}
		2760	7.90×10^{3}

The boundary between the ingot base and top surface of the graphite starter block has been treated as a contact interface with a no-slip friction condition.

Since differential volumetric contraction/expansion within the silicon and graphite block drives the formation of differential strains leading to the residual stresses, the correct description of the thermal dilatational behaviour is critical to the model. The thermal-linear strain of silicon or graphite, ε_{th} (T), at temperature T, relative to some datum T_0, can be calculated via the following expression:

$$\varepsilon_{\text{th}}(T) = \int_{T_0}^{T} \alpha(T)\,\mathrm{d}T \tag{13}$$

where α is the dilatation or expansion coefficient for each material. ABAQUS requires as input the reference temperature for zero strain and the thermal expansion coefficient calculated based on the total strain ε_{th} at temperature T relative to the reference temperature, input in a tabulated format. The reference temperature for the silicon is taken to be 1400 °C, the silicon solidus point. The thermal expansion due to solidification of the silicon, approximately 9.5% [9], has been ignored, as it is assumed the newly solidified material is free to expand into the liquid. The same reference temperature of 1400 °C was also chosen for the graphite as the initial layer of silicon which forms on the graphite will be strain free. The variation in thermal strain with temperature for silicon and graphite used in this investigation are shown in Fig. 7.

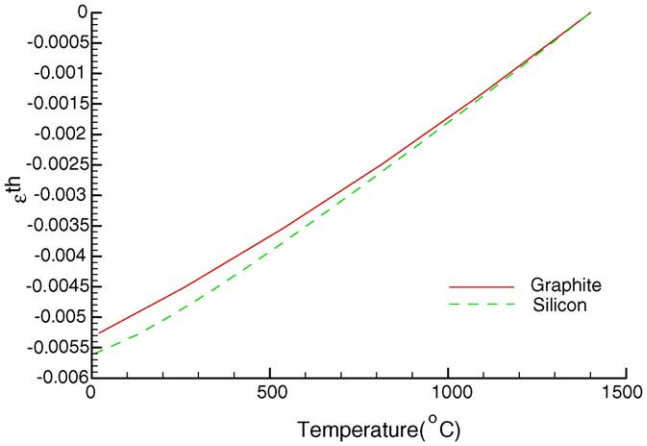

Fig. 7. Thermal contraction behaviour of silicon and graphite relative to 1400 °C [14,18].

4. Results and discussion

4.1. Results of thermal analysis

4.1.1. Graphite preheat analysis

For the purpose of evaluating some of the boundary conditions in the model an initial experiment was conducted in which only the graphite was heated (no silicon was charged to the mould). Fig. 8 shows a comparison between the measured and predicted temperatures at the location of the thermocouples, following trial and error adjustment of boundary conditions exhibiting the greatest sensitivity, to obtain the "best fit". TC-#1 and TC-#2 were located in the graphite 17 and 23 mm from the heated surface, respectively (refer to Fig. 3). The variation in beam power has also been plotted for comparison. The predicted temperature responses show the correct trends and clearly exhibit sensitivity to the changes in applied EB power. The model under predicts rate of temperature increase and the predicted steady-state temperature gradient is smaller than that measured. Possible causes for the deviation

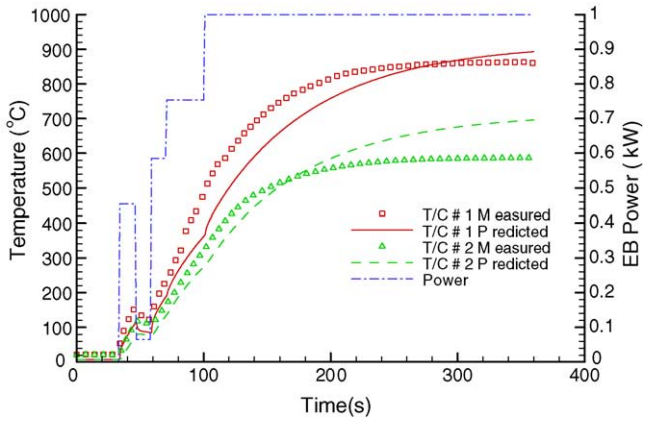

Fig. 8. Comparison of measured and predicted temperatures for a preheat EB power of 1000 W at two locations in the graphite starter block (referring to Fig. 3).

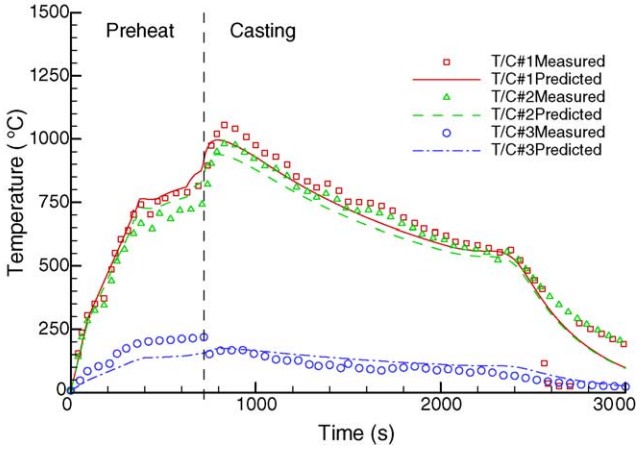

Fig. 9. Comparison of measured and predicted temperature for Casting 1 (3.8 kW EB power and 2 mm/min casting rate).

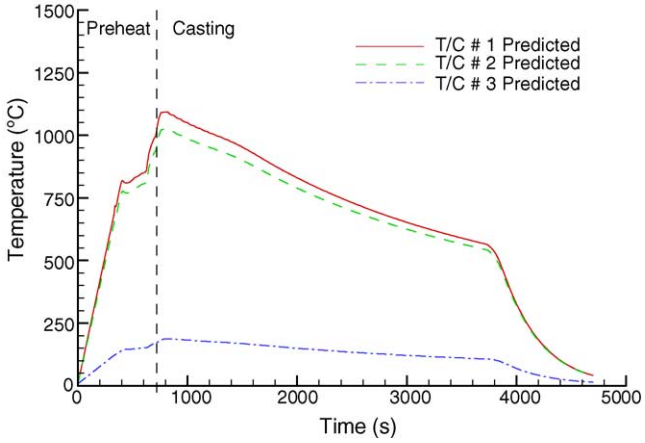

Fig. 10. Predicted temperatures for Casting 2 (3.8 kW EB power and 1 mm/min casting rate).

of the predictions from the measurements are differences in the thermo-physical properties, errors in the quantification of the boundary conditions or errors in the measurement.

4.1.2. Silicon casting analysis

The thermocouple data obtained from Casting 1 (3.8 kW, 2 mm/min) is presented in Fig. 9 (the pyrometer data has not been include because of problems encountered with excessive noise). The model predictions at locations consistent with the position of the thermocouples, as well as, the centerline surface temperatures, have also been included for comparison. As can be seen there is an increase in the temperature measured by all three thermocouples during the preheating phase. The current standard casting practice is to preheat the graphite starter block at a reduced EB power prior to the start of casting. The temperature then decreases as casting begins or shortly after, depending on the EB power input. The measured temperatures in the graphite are fairly close in magnitude, peaking at between 980 and 1050 °C, but show a general trend to decreasing temperature with increasing distance from the casting/starting block interface, as would be anticipated. The temperature measured in the water-cooled copper support is significantly lower in magnitude, peaking at ∼220 °C. The decrease in temperature with increasing cast length is consistent with the increasing thermal resistance offered by the silicon ingot in proportion to the cast length. Overall, the model predictions in the graphite and copper sections exhibit satisfactory agreement with the measured temperatures.

The thermal model was used to predict the temperature evolution in ingots produced with processing conditions consistent with Castings 2 and 3. The same preheat condition employed for Casting 1 was used for Castings 2 and 3. The temperature predictions for Castings 2 and 3 at the same locations presented in Fig. 9 are presented in Figs. 10 and 11. As expected, the preheat temperature predictions are the same for all three casting conditions. Overall, temperature evolution at the thermocouple locations shows the same trends for each casting condition. However, the slow withdrawal rate exhibited by Casting 2 required double the casting time to produce a 56 mm ingot. The peak temperatures, occurring just after cast start, at thermocouple location #1 are predicted to be 1000, 1091, and 1012 °C for Castings 1–3, respectively.

The thermal model predictions have also been used to estimate the sump depth at the ingot center as a function of cast length in the three ingots, shown in Fig. 12. The sump depth increases with increasing cast height until the solidification temperature at the centerline is reached and the sump begins to move upward. The sump profile and the evolution of the sump depth exhibit limited dependency to the processing conditions examined. The increased EB power in Casting 3 has resulted in a 1mm increase in the sump depth. The decreased withdrawal rate employed in Casting 2 has no effect on the final sump depth of 21 mm when compared with Casting 1.

4.2. Residual stress data and predictions

As previously described, the predicted temperatures for each of the casting conditions were used as input to the stress model. To allow comparison to the residual strain

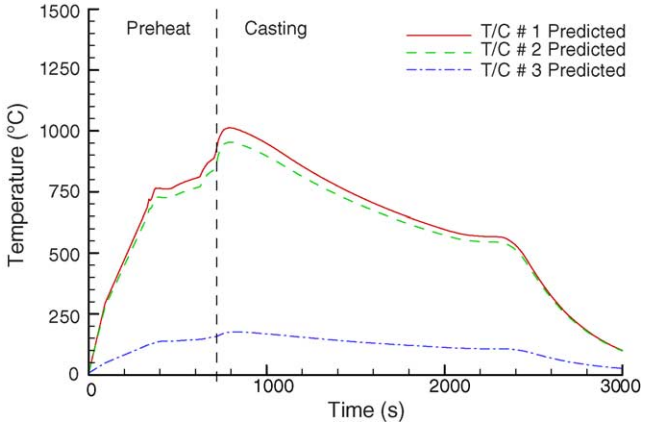

Fig. 11. Predicted temperatures for Casting 3 (5 kW EB power and 2 mm/min casting rate).

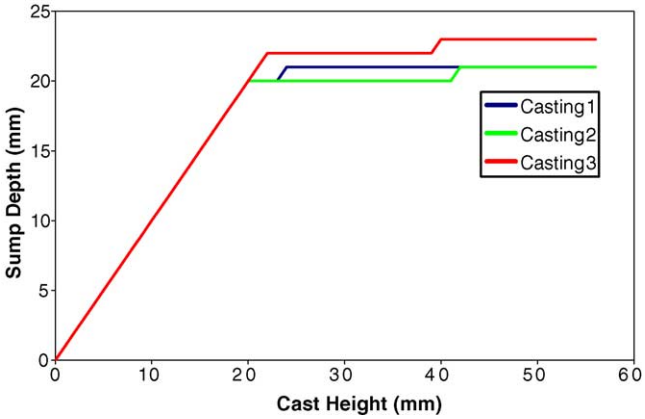

Fig. 12. Predicted sump depth vs. cast height for the three experimental casting conditions.

measurements the strains output from the model are the elastic strains predicted to be present at the end of the casting process when the ingot and starter block have been cooled to room temperature. The resulting strains in the radial, axial and hoop orientations, predicted by the model, have been plotted for Castings 1, 2 and 3 as a function of height in the ingot (0 mm corresponds to the base of the casting) in Figs. 13–15, respectively. The profile of strain with height has been output from the model at three radial locations 15, 17 and 19 mm which lie close to the surface of the casting (located at 20 mm). This data has been plotted together with the results from the neutron diffraction measurements (in micro strain) for all three castings at the same radial locations.

Turning first to the measurements, the estimated uncertainty in the strain measurements has been shown as error bars at each point in Figs. 13–15. The relatively large uncertainty in the measured data makes it difficult to interpret. In general, the trend in the measurements is one of compressive (−) strain at the radial positions examined, with only a few exceptions at specific locations—a couple of which are in proximity to the ingot base. This result is consistent with expectations, as the outer regions of the casting will experience tensile (+) stresses at elevated temperatures as the surface is cooled. These tensile stresses will be of sufficient magnitude (at the high temperatures) to result in plastic flow and the accumulation of plastic tensile strain leading to a general expansion of the outer near-surface region of the casting relative to the inner, near-centre regions. This outer "expanded" region will then be placed in compression as the ingot cools to room temperature resulting in the compressive strains observed. The mechanism for development of residual strain is similar to that observed in glass tempering.

Based on an overall view of the data there is enough evidence to conclude that the hoop strains are in general the largest in magnitude, followed by the axial and radial strains. There does not appear to be any other trends in the variation of strain with height or radius that are consistent across all three castings owing to the scatter in the data.

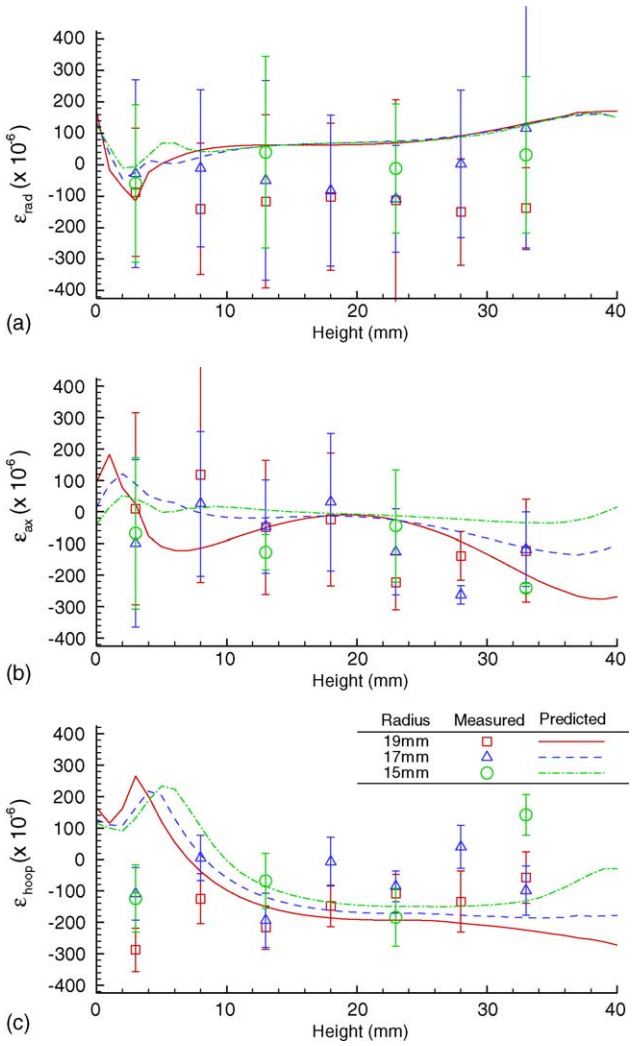

Fig. 13. Comparison of measured (symbols) and predicted (lines) residual microstrains in the (a) radial, (b) axial, and (c) hoop orientations along the length of Casting 1 at three locations near the surface.

The model predictions for strain by and large indicate transition regions at either end of the casting and a steady state region in the centre, which is consistent with the behaviour of the process from a thermal standpoint. More specifically, the hoop and axial residual strains are predicted to be tensile in proximity to the ingot base, they then transition to compression within the first 10 mm from the base where they remain roughly constant until at the top where they tend to vary with height (at the 19 mm radius location the compressive strain intensifies and at 15 mm location the strain tends to fall off). The radial strains behave differently and start off in compression near the base, transition to tension within the first 10 mm and then gradually increase with increasing height in the casting.

Overall the level of agreement between the model predictions and the measurements is satisfactory and within the uncertainty in the measurements. The discrepancy at the base of the ingot, where the model predicts the wrong sign in the hoop and axial strains (they are predicted to be tensile,

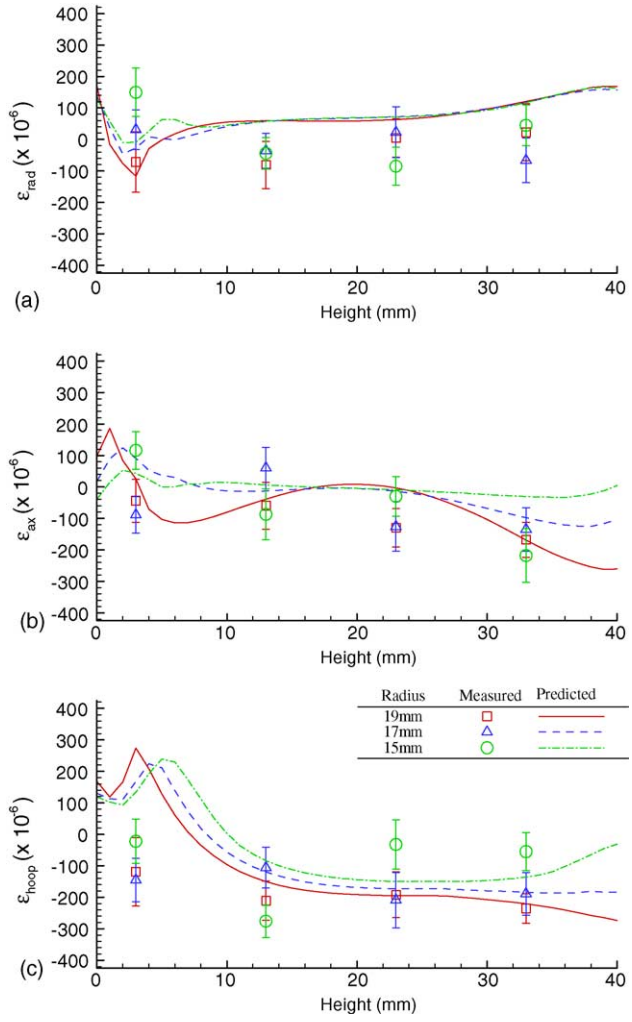

Fig. 14. Comparison of measured (symbols) and predicted (lines) residual microstrains in the (a) radial, (b) axial, and (c) hoop orientations along the length of Casting 2 at three locations near the surface.

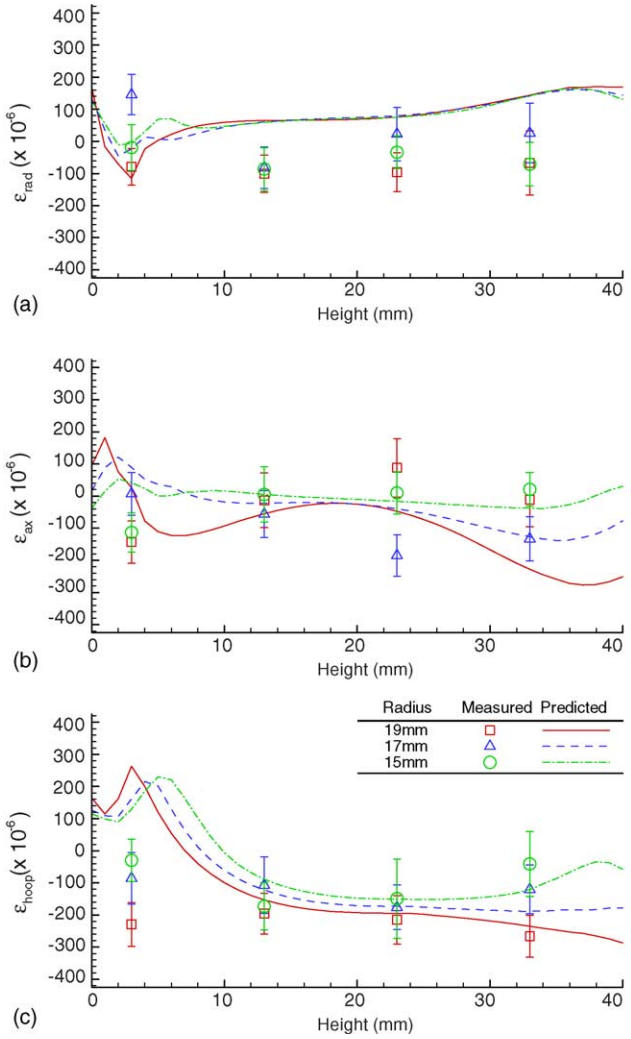

Fig. 15. Comparison of measured (symbols) and predicted (lines) residual microstrains in the (a) radial, (b) axial, and (c) hoop orientations along the length of Casting 3 at three locations near the surface.

whereas the measurements indicate they are compressive) may be attributed to the no-slip boundary condition chosen for this interface which is likely too rigid. The introduction of some slip could reduce the tensile strains to bring them more inline with the measurements.

If the predictions at the ingot base are ignored, then in one instance, Fig. 15(c), the level of agreement between the model predictions and measurements is actually very good. The predictions show good quantitative agreement in terms of variation in strain with both ingot height and also radial position at the majority of the locations examined including the transient region at the top of the casting. The tendency to predict higher strains closer to the ingot surface (at 19 mm radius) than at greater depths below the surface (at 15 mm) is consistent with expectations, as the outer surface should experience a higher temperature gradient, thermal-stress and magnitude of plastic tensile strain at temperature, giving rise to a higher compressive strain at room temperature. Unfortunately, for the other castings and strain orientations the good overall agreement seen in Fig. 15(c) is not reproduced; albeit there is good agreement at a few specific locations. At best there is reasonable overall qualitative agreement in the case of the hoop and axial strains only (in the case of the radial strains they are predicted to be tensile at most locations whereas the measurements indicate they should be compressive).

Factoring in the ability of the model to correctly predict the distribution of strain in one case quantitatively (as well as at several discrete locations in other cases), the magnitude of the uncertainty in the measurements and ignoring the predictions in proximity to the base (where the mechanical boundary condition is arguably too restrictive) then we may conclude that the model is likely adequate to assess process trends qualitatively. On the basis of this, the influence of EB beam power and withdrawal rate on the residual stress state can be assessed. Fig. 16 compares the predicted residual microstrain results at the surface of Castings 2 and 3 against the

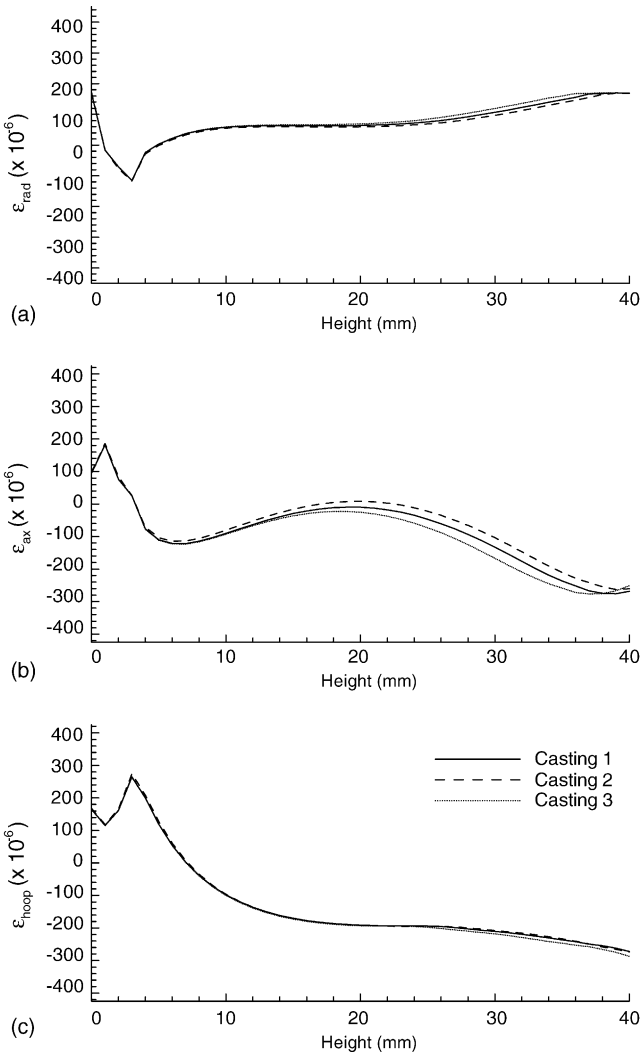

Fig. 16. Comparison of predicted residual microstrains in the (a) radial, (b) axial, and (c) hoop orientations along the length of Castings 1 (solid line), 2 (dashed line) and 3 (dotted line) at the surface.

base case, Casting 1. This comparison indicates that increasing the withdrawal speed and increasing EB power have little effect on the final strain distributions, which is consistent with the fact that they also have only a limited effect on the overall process heat transfer as indicated from the pool depth sensitivity. The reason for this behaviour can be understood by looking at the way in which the boundary condition describing heat transfer to the mould is quantified in the model—see Eq. (9) and Table 3. As defined, the regions characterized as meniscus cooling and limited contact cooling are temperature dependent. Increasing the temperature in the molten pool through an increase in EB power or by increasing the withdrawal rate will result in changes in heat transfer that will tend to offset the imposed change—e.g. the lengths within the mould over which these heat transfer regimes are operating will increase with increasing temperature tending to draw out more heat and offset the imposed change. From a process control standpoint, the lack of sensitivity of strain to these process parameters is good as these parameters are critical to controlling melting and refining.

It remains to be determined if the levels of micros strain predicted by the model are detrimental to the fabrication of solar-cells from this material. If so, some type of annealing step may be required prior to cutting the ingot.

5. Conclusions

A technique based on EBMR has been used to refine N-type scrap silicon for the purpose of producing material suitable for photovoltaic applications. In an effort to understand the influence of processing parameters on residual stress distribution in the final ingot, castings were produced at two levels of EB power and two levels of withdrawal speed. During casting, temperatures in the graphite starter block and copper support were measured for each casting. The residual strain in each ingot was measured using the neutron diffraction technique. A sequentially coupled thermal-stress model was developed using the commercial FE software ABAQUS. User-written subroutines were used to describe the complex heat transfer phenomena active in this process.

Overall, the model adequately describes the development of residual strain in the ingots under the processing conditions employed. Based on the measured and predicted strains, it is clear that ingots produced using this casting technique contain considerable residual strain. It is possible that cracking will occur during subsequent processing or that considerable deformation with occur when the ingots are sectioned into thin gauge samples. Further, attempts to use processing conditions to reduce residual strain indicate that increased EB power and reduced withdrawal rate have little effect on the resulting residual strain. Further investigations are planned to determine new processing routes to reduce the final residual strain.

Acknowledgement

The authors gratefully acknowledge access to facilities provided by the National Research Council of Canada through the Neutron Program for Materials Research.

References

[1] Tetsu-to-Hagane, vol. 71, 1985, p. 170.
[2] PV News, vol. 19, 2000.
[3] K. Suzuki, T. Kumagai, N. Sano, ISIJ Int. 32 (1992) 630–634.
[4] K. Sakaguchi, M. Maeda, Metall. Trans. B 23B (1992) 423–427.
[5] S. Suhara, N. Yuge, M. Fukai, F. Aratani, CAMP-ISIJ 2 (1989) 1341.
[6] N. Yuge, Research of manufacturing techniques of high purity silicon for solar cell, University of Tokyo, 1997.
[7] T. Ikeda, M. Maeda, ISIJ Int. 32 (1992) 635–642.

[8] M. Mauk, JOM 55 (2003) 38–42.
[9] R.A. Logan, W.L. Bond, J. Appl. Phys. 30 (1959) 322.
[10] M.T. Hutchings, A.D. Krawitz (Eds.), Measurement of Residual and Applied Stress Using Neutron Diffraction, Kluwer Academic Publishers, Dordrecht, 1992.
[11] E. Koleva, K. Vutova, G. Mladenov, Vacuum 62 (2001) 189–196.
[12] M.A. McClelland, K.W. Westerberg, T.C. Meier, D.G. Braun, L.V. Berzins, T.M. Anklam, in: R. Bakish (Ed.) Electron Beam Melting and Refining—State of the Art 1996, Bakish Materials Corporation, Reno, 1996, pp. 151–62.
[13] M. Ritchie, P.D. Lee, A. Mitchell, S.L. Cockcroft, T. Wang, Metall. Mater. Trans. A 34A (2003) 863–877.
[14] R. Hull (Ed.), Properties of Crystalline Silicon, vol. 20, The Institute of Electrical Engineers, London, 1999.
[15] O.C. Zienkiewicz, R.I. Taylor, The Finite Element Method, fourth ed., McGraw-Hill Book Co., New York, 1994.
[16] Orton Refractory Testing and Research Center, unpublished.
[17] F.M. White, Heat and Mass Transfer, Addison-Wesley Publishing Company, New York, 1991.
[18] E.J. Seldin, Carbon 4 (1966) 177–191.
[19] H. Siethoff, H.G. Brion, Philos. Mag. A 81 (2001) 145–152.